Morphology Control of Cryptomelane Type MnO_2 Nanowires by Soft Chemistry. Growth Mechanisms in Aqueous Medium

David Portehault,[†] Sophie Cassaignon,*[,†] Emmanuel Baudrin,[‡] and Jean-Pierre Jolivet[†]

Chimie de la Matière Condensée de Paris, UMR CNRS 7574, Université Pierre et Marie Curie-Paris6, cc 174, 4 place Jussieu, 75005 Paris, France, and Laboratoire de Réactivité et Chimie des Solides, UMR CNRS 6007, Université de Picardie-Jules Verne, 33 rue Saint-Leu, 80039 Amiens cedex, France

Received June 20, 2007. Revised Manuscript Received July 27, 2007

Nanowires of one-dimensional manganese oxide (cryptomelane) have been synthesized using reaction between Mn^{II} ($MnSO_4$) and Mn^{VII} ($KMnO_4$) in water by a low-temperature route at 60 °C and 95 °C. Characterization of the nanoparticles was carried out using powder X-ray diffraction, transmission electron microscopy, electron diffraction, and nitrogen adsorption−desorption. Two synthesis methods were developed depending whether the pH was initially adjusted or fixed all along the solid formation. Both methods exhibited variation of the nanowire morphology with diameter, length, and specific area varying in the 15−40 nm, 0.1−1.1 μm, and 35−110 $m^2 \cdot g^{-1}$ ranges, respectively, depending on the growth conditions (acidity and temperature). The growth mechanism of the nanowires was proved to proceed by oriented attachment of primary 10 nm width nanorods for the lateral direction and dissolution−crystallization for the longitudinal direction. The diameter variation with acidic conditions was interpreted in terms of electrostatic interactions between primary nanorods.

Introduction

Nanoscale morphologies are nowadays attractive owing to their unique optical, magnetic, mechanical, and electronic properties.[1] Among them, low dimensionality nanostructures, for instance, one-dimensional (1D), exhibit specific behavior. Many synthetic routes have been investigated to form such 1D morphologies such as sol−gel process, precipitation, chemical vapor deposition, laser ablation, or template-directed crystallization.[1,2] Furthermore, as many properties (e.g., electrochemical, mesogenic, or catalytic) depend on the particle size (i.e., diameter and length), the precise control of the morphology and the texture remains an important challenge for tuning the properties.

Tunnel-based manganese oxides (TMO) are microporous mixed valent (III, IV) manganese oxides.[3] Their structures are made of edge-shared MnO_6 octahedra forming chains linked together by corners of MnO_6 octahedra. This connectivity thus allows the formation of 1D tunnel structures with $X \times X$ octahedra cross sections ($X = 1$, 2, 3, or 4). Cryptomelane-type manganese oxides (TMO-2) are formed of 2×2 tunnels 0.46 nm in size (Figure 1). These are usually stabilized by water molecules and small amounts of various cations such as alkaline (K^+ cryptomelane K-TMO-2),[3] alkaline-earth (Ba^{2+} hollandite Ba-TMO-2 naturally occurring form),[3,4] or metal ions (Cu^{2+}).[5,6] TMO-2 are intensively studied because of their application in catalysis,[7,8] separation[9] (the term "octahedral molecular sieves", OMS, is sometimes used),[4] ion sensing,[10] and energy storage applications.[11,12]

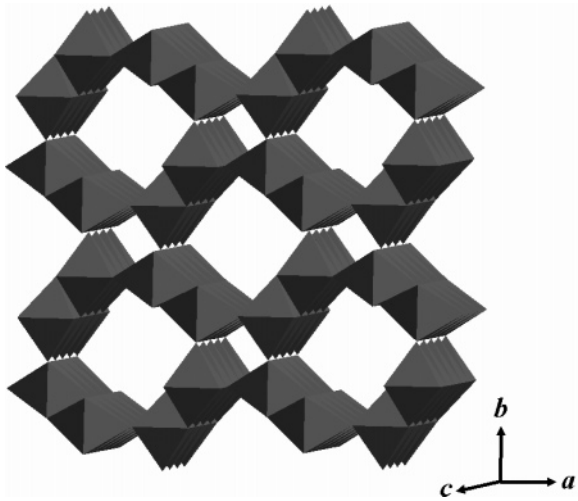

Figure 1. Crystalline MnO_6 framework of cryptomelane type manganese oxides.

* To whom correspondence should be addressed. E-mail: cassai@ccr.jussieu.fr.
[†] Université Pierre et Marie Curie-Paris6.
[‡] Université de Picardie-Jules Verne.

(1) Burda, C.; Chen, X.; Narayanan, R.; El-Sayed, M. A. *Chem. Rev.* **2005**, *105*, 1025−1102.
(2) Xia, Y.; Yang, P.; Sun, Y.; Wu, Y.; Mayers, B.; Gates, B.; Yin, Y.; Kim, F.; Yan, H. *Adv. Mater.* **2003**, *15*, 353−389.
(3) Post, J. E. *Proc. Natl. Acad. Sci. U.S.A.* **1999**, *96*, 3447−3454.
(4) Liu, J.; Makwana, V.; Cai, J.; Suib, S. L.; Aindow, M. *J. Phys. Chem. B* **2003**, *107*, 9185−9194.
(5) De Guzman, R. N.; Shen, Y. F.; Neth, E. J.; Suib, S. L.; O'Young, C. L.; Levine, S.; Newsam, J. M. *Chem. Mater.* **1994**, *6*, 815−821.
(6) Chen, X.; Shen, Y.-F.; Suib, S. L.; O'Young, C. L. *Chem. Mater.* **2002**, *14*, 940−948.
(7) Ding, Y.-S.; Shen, X.-F.; Sithambaram, S.; Gomez, S.; Kumar, R.; Crisostomo, V. M. B.; Suib, S. L.; Aindow, M. *Chem. Mater.* **2005**, *17*, 5382−5389.
(8) Jothiramalingam, R.; Viswanathan, B.; Varadarajan, T. K. *Catal. Commun.* **2005**, *6*, 41−45.
(9) Feng, Q.; Kanoh, H.; Miyai, Y.; Ooi, K. *Chem. Mater.* **1995**, *7*, 148−153.
(10) Sauvage, F.; Baudrin, E.; Tarascon, J.-M. *Sens. Actuators, B* **2007**, *120*, 638−644.
(11) Thackeray, M. M. *Prog. Solid State Chem.* **1997**, *25*, 1.
(12) Kijima, N.; Takahashi, Y.; Akimoto, J.; Awaka, J. *J. Solid State Chem.* **2005**, *178*, 2741−2750.

10.1021/cm071654a CCC: $37.00
Published on Web 09/29/2007

During the last 5 years, solvent free,[7] sol−gel[13] or ionic liquid route,[14] hydrothermal[15,16] or aqueous route under refluxing conditions implying Mn^{2+} oxidation,[17] MnO_4^- reduction,[18] or Mn^{2+}/MnO_4^- comproportionation[17] have been developed to obtain 1D TMO-2 nanoparticles. The diameter often ranged between 30 and 100 nm with length varying from few hundreds of nanometers to a few micrometers. Usually TMO-2 crystallization proceeds through two steps: first, a disordered[18] or layered[18−20] manganese oxide precursor is formed, which then transforms into 1D TMO-2 under aging. Such a process recently allowed Villegas et al. to first obtain K-TMO-2 nanowires with diameters in the 6−20 nm range.[18] Synthesis was performed in aqueous acidic conditions under reflux and with varying oxidizing ($KMnO_4$) and reducting (H_2O_2) agent concentrations. Size variation was explained in terms of the solid precursor nucleation rate, but the TMO-2 growth mechanism was not further investigated. To the best of our knowledge, no intensive study has focused on the growth mechanisms of MnO_2 nanowires, despite many studies which have proved the aging solution route conditions to be of significant impact on the final oxide nanoparticle morphology. Growth mechanisms have often been invoked to explain size control of oxide nanoparticles. Coarsening (Ostwald ripening)[21−23] and oriented attachment[24−29] are the main processes that have been highlighted. Nevertheless, few reports deal with the growth mechanisms and size tailoring of 1D oxide nanoparticles via a solution route.[25−27] Thus, a better understanding of TMO-2 nanowires formation and growth mechanisms could provide a base to understand 1D oxide nanoparticles formation. Especially, improved morphology control should be provided by considering not only the nucleation step but also the whole process of crystallization.

This report addresses a low temperature (60−95 °C) aqueous route for the precipitation of K-TMO-2 nanowires. Soft conditions permit fine-tuning of the reaction path and control of the particle diameter and length in the 15−40 nm and 100−800 nm ranges, respectively. First, the TMO-2 nucleation from a disordered precursor is studied. Second, size and morphology tuning of the nanowires is evidenced. Finally, the nanoparticles growth process is discussed, and an original mechanism is highlighted which is proved to proceed via primary nanorod oriented attachment and dissolution−crystallization.

Experimental Section

Synthesis. K-TMO-2 has been synthesized using comproportionation between Mn^{2+} and MnO_4^- in water and in stoichiometric ratio according to the following reaction:

$$2MnO_4^- + 3Mn^{2+} + 2H_2O \rightarrow 5MnO_2 + 4H^+$$

$MnSO_4$, H_2O (30 mmol, Aldrich), and $KMnO_4$ (20 mmol, Aldrich) were dissolved respectively in 75 mL and 150 mL of aqueous H_2SO_4 solution with the same pH ranging from 6.0 to 0.0. Two procedures were used:

Method A. After nitrogen bubbling during 30 min, the $KMnO_4$ solution was added to the $MnSO_4$ one under vigorous stirring and nitrogen bubbling. The addition rate was 1.25 mL·s^{-1}, and mixing was completed after 2 min. The volume was adjusted to 250 mL with a solution of the same acidity as the initial one. A black precipitate appeared immediately, and the pH fell dramatically. To investigate the pH influence on the aging process, method B was also used.

Method B. Several syntheses have been performed using the same procedure as method A except that a stationary pH value was fixed all along the synthesis using a 808 Titrando Metrohm unit by regulated addition of 2 mol·L^{-1} KOH solution. Mixing was completed after 45 min.

For both procedures, suspensions were aged in a stove at 25, 60, or 95 °C for 7 days and shaken once per day. pH did not change during aging. Samples were collected at different times (on a duration of 7 days) and centrifuged. The powders were washed twice with deionized water and first dried at room temperature under nitrogen flux. Then they were dried in a stove at 95 °C overnight. The reaction is quantitative and yields approximately 4 g of solid.

Techniques. *MnO_4^- and Mn^{2+} Titration.* Linear scan hydrodynamic voltammetry was used with a rotating platinum disc as the working electrode, a saturated calomel electrode (SCE) as a reference, and platinum as the counter electrode. The rotation speed was 400 rpm. The analyzed solution was diluted 10 times in the supporting electrolyte solution (HNO_3 1 mol·L^{-1}) saturated with argon bubbling. Two linear scans at a 10 mV·s^{-1} sweep rate were carried out from 0.5 to 1.5 V versus SCE and from 1.4 to 0.7 V to determine the Mn^{2+} and MnO_4^- concentrations, respectively. Limiting currents were measured, and concentrations were evaluated from calibration curves ($I_l(A) = 1.86 \times 10^{-1}[Mn^{2+}]$ (mol·L^{-1}) and $I_l(A) = 6.34 \times 10^{-2}[MnO_4^-]$ (mol·L^{-1}), respectively).

Mn Average Oxidation State (AOS) Determination. The AOS was determined using the following procedure. A total of 30 mg of particles were dispersed in 4.0 mL of 0.50 mol·L^{-1} ammonium iron(II) sulfate, 6 mL of concentrated sulfuric acid, and 10 mL of deionized water. The suspension was stirred for 1 h until particles were completely dissolved. Then it was transferred in a 50 mL volumetric flask which was completed with deionized water. A blank test without particles was performed to correct Fe(II) oxidation by air. Two 5.0 mL samples were taken. The first was titrated with a 1.0×10^{-2} mol·L^{-1} $K_2Cr_2O_7$ aqueous solution to

(13) Ching, S.; Roark, J. L.; Duan, N.; Suib, S. L. *Chem. Mater.* **1997**, *9*, 750−754.
(14) Yang, L.-X.; Zhu, Y.-J.; Wang, W.-W.; Tong, H.; Ruan, M.-L. *J. Phys. Chem. B* **2006**, *110*, 6609−6614.
(15) Giovanoli, R.; Rossman, G. R. *Chimia* **1981**, *35*, 53.
(16) Feng, Q.; Yanagisawa, K.; Yamasaki, N. *Chem. Commun.* **1996**, *14*, 1607−1608.
(17) Wang, X.; Li, Y. *Chem. Commun.* **2002**, *7*, 764−765.
(18) Villegas, J. C.; Garces, L. J.; Gomez, S.; Durand, J. P.; Suib, S. L. *Chem. Mater.* **2005**, *17*, 1910−1918.
(19) Shen, X.-F.; Ding, Y.-S.; Hanson, J. C.; Aindow, M.; Suib, S. L. *J. Am. Chem. Soc.* **2006**, *128*, 4570−4571.
(20) Wang, X.; Li, Y. *Chem.—Eur. J.* **2003**, *9*, 300−306.
(21) La Mer, V. K.; Dinegar, R. H. *J. Am. Chem. Soc.* **1950**, *72*, 4847−4854.
(22) Jolivet, J.-P.; Chanéac, C.; Tronc, E. *Chem. Commun.* **2004**, 481−487.
(23) Jolivet, J.-P. *Metal Oxide Chemistry and Synthesis. From Solution to Solid State*; Wiley: Chichester, 2000.
(24) Penn, L. R.; Banfield, J. F. *Science* **1998**, *281*, 969−971.
(25) Huang, F.; Zhang, H.; Banfield, J. F. *Nano Lett.* **2003**, *3*, 373−378.
(26) Adachi, M.; Murata, Y.; Takao, J.; Jiu, J.; Sakamoto, M.; Wang, F. *J. Am. Chem. Soc.* **2004**, *126*, 14943−14949.
(27) Pacholski, C.; Kornowski, A.; Weller, H. *Angew. Chem., Int. Ed.* **2002**, *41*, 1188−1191.
(28) Zhang, D.-F.; Sun, L.-D.; Yin, J.-L.; Yan, C.-H. *Adv. Mater.* **2003**, *15*, 1022−1025.
(29) Banfield, J. F.; Welch, A. S.; Zhang, H.; Thomsen, Ebert, T.; Penn, L. R. *Science* **2000**, *289*, 751−754.

determine the Fe^{2+} excess. The second one was introduced in a 250 mL beaker with 10 mL of water, 10 mL of concentrated nitric acid, 5 mL of concentrated H_3PO_4, and 1.2 g of KIO_4. The mixture was heated at 95 °C under stirring until it turned to deep pink. The solution was cooled and diluted with an appropriate volumetric flask. The solution absorbance was then measured at the 525 nm wavelength, and the total manganese quantity could be determined using a calibration curve (ϵ(525 nm) = 2323 mol^{-1}·L·cm^{-1}). The two independent experiments made it possible to evaluate the Mn^{III} and Mn^{IV} proportions.

Elemental Analysis. K and Mn elemental ratios were determined at the CNRS Service Central d'Analyse, USR 59, by inductively coupled plasma atomic emission spectroscopy (ICP-AES). Both AOS determination and elemental analysis enabled the determination of K, Mn, O, and H_2O compositions.

X-ray Diffraction (XRD). Powder XRD measurements were performed with a Philips PW1050/25 X-ray diffractometer operating in the reflection mode at Cu Kα radiation with 40 kV beam voltage and 20 mA beam current. The data were collected in the 8−80° range (2Θ) with steps of 0.02° and a counting time of 10 s. Crystallite apparent mean diameter was determined using the Debye−Scherrer equation with the integral breadths corrected for the instrumental broadening. The (110), (200), (220), and (310) peaks of cryptomelane were exploited.[30] For each diffraction pattern, strains have been verified to be a minor cause for line broadening.[31] As a result, it seems essentially due to the size effect.

Transmission Electronic Microscopy (TEM). The nanoparticles morphology and orientation were studied by TEM and high-resolution TEM (HRTEM) using JEOL 100 CX (100 kV) and Philips CM20 (200 kV) apparatus. Samples were prepared by evaporating a drop of aqueous diluted suspension on a carbon-coated copper grid. The *d*-spacings obtained from the selected area electron diffraction (SAED) pattern were calibrated using the Au pattern. Size distributions were determined by measuring the average diameter of 200 particles for diameters and 150 particles for lengths. Histogram plots (Supporting Information) were used to check the profiles to be gaussians, and then mean values were reported with an experimental error of approximately 5%. Standard deviations were also evaluated and are interpreted as polydispersity indicators.

Specific Area Measurements (S_{BET}). Specific surface areas were determined using an ASAP 2010 Micrometrics apparatus following the BET analysis. Adsorption and desorption of N_2 were performed at 77 K. Samples had been previously outgassed by heating at 120 °C overnight under a 3 μm Hg pressure.

Results

(1) Nucleation and Phase Ordering. K-TMO-2 has been synthesized using reaction between Mn^{2+} and MnO_4^- in water according to the reaction described in the experimental section. Two procedures were used. In the first one, denoted method A, the initial pH is adjusted at a fixed value, but pH was free to vary during aging. In the second one, denoted method B, the pH is maintained at a fixed value all along the synthesis.

When the $KMnO_4$ solution is added to the $MnSO_4$ one, the system turns immediately light brown and darkens during the addition. A black precipitate is finally obtained. Its AOS has been evaluated to 3.96. Supernatant voltammetric titration indicated that more than 99% of $KMnO_4$ and 91% of $MnSO_4$ had reacted 10 min after the reagents mixing. The reaction is completed after aging 1.5 h at 95 °C. For method A, pH falls dramatically up to around 1 during the addition as expected from the equation described previously. Therefore several experiments were performed with method B which afford a constant pH value. The evolution in suspension of the precipitate was studied by powder XRD (Figure 2). XRD patterns indicate that initial precipitates are poorly ordered, and aging at 25 °C causes no evolution. At higher temperature (60 or 95 °C), characteristic peaks of K-TMO-2 appear after a few hours of evolution of the solids obtained by both methods for pH ≤ 2. High acidity seems to increase the kinetics of phase transformation. The XRD patterns of the solid obtained after 1 week can be indexed in the *I*4/*m* space group with a = 0.9805(4) nm and c = 0.2849(2) nm. The mean AOS measured after aging for 7 days is 3.79. It is lower than for the early precipitate, what could be due to K^+ insertion during the ordering of the early precipitate. The mean composition evaluated from AOS determination and elemental analysis is $K_{0.11}MnO_{1.85}\cdot(H_2O)_{0.75}$, which is consistent with previous reports and confirms that K-TMO-2 is obtained.[18] No systematic variation of cell parameters, AOS, potassium, and water content with pH or temperature was observed. With method B, for pH > 2, the early precipitate does not transform into cryptomelane. The pattern obtained after 1 week is attributed to the layered manganese oxide birnessite.[32]

TEM and SAED show that the early precursor exhibits crumpled paper morphology with both methods (Figure 3).

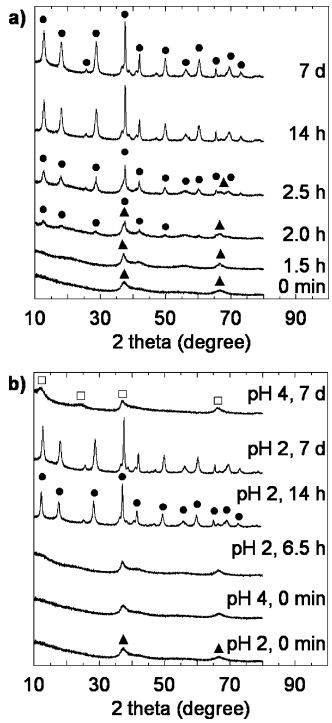

Figure 2. Powder XRD patterns obtained after different aging times: disordered early precipitate (▲), cryptomelane (●), and birnessite (□). Method A: initial pH 1.3 and aging at 95 °C (a). Method B: stationary pH 2.0, aging at 95 °C, and stationary pH 4.0, aging at 95 °C (b).

(30) JCPDS 42-1348.

(31) Klug, H. P.; Alexander, L. E. *X-ray Diffraction Procedures for Polycrystalline and Amorphous Materials*; Wiley: New York, 1974.

(32) JCPDS 80-1098.

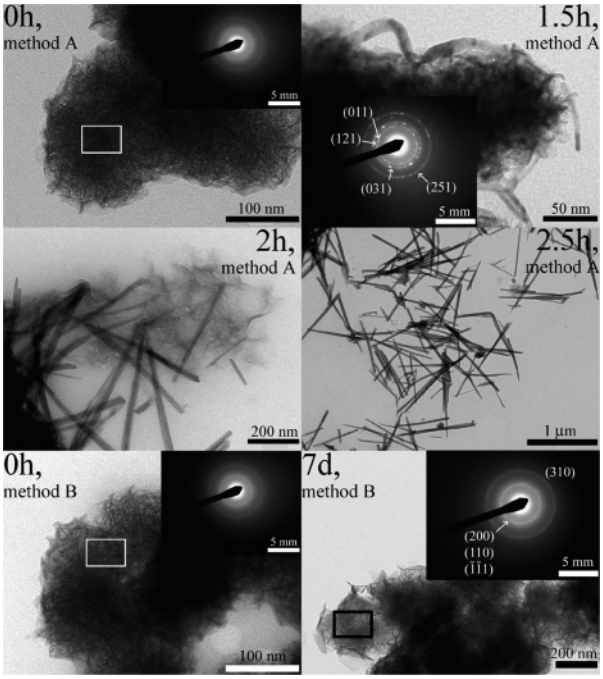

Figure 3. TEM micrographs during the phase transformation from the disordered precursor (initial samples from methods A and B). Evolution toward the cryptomelane nanowires (2.5 h) obtained with method A, initial pH 1.3 (final pH 1.0) at 95 °C. SAED pattern exhibiting characteristic distances of the cryptomelane structure is obtained after 1.5 h of aging. Evolution toward birnessite (7 days) obtained with method B, stationary pH 4, at 95 °C.

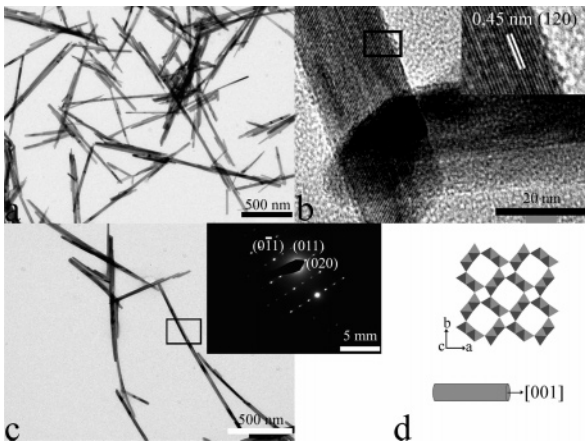

Figure 4. TEM micrographs (a, c), HRTEM (b), and SAED (c, inset) of cryptomelane nanowires obtained with synthesis method A, initial pH 1.3 (final pH 1.0), after aging 7 days at 95 °C. Indexed longitudinal axis of the nanowires (d).

The early solid evolves to nanowire type particles after 2.5 h (Figure 3) for method A, with a SAED pattern exhibiting characteristic distances of the K-TMO-2 structure. The micrograph obtained at 1.5 h indicates that nanowires seem to nucleate from the early precursor particles. Phase evolution with method B at pH ≤ 2 (not shown) is strongly similar to that observed with method A. At pH > 2, birnessite exhibiting the same morphology as the precursor one is obtained.

(2) Cryptomelane Morphology. TEM analysis performed for different synthesis conditions shows that the diameter of the nanowires ranges from 18 to 36 nm while length ranges from 100 to 800 nm when varying acidity and temperature. HRTEM (Figure 4b) indicates good alignment of the (120) planes along the nanowire axis. The SAED pattern (Figure 4c, inset) can be indexed in the *I*4/*m* space group, which is consistent with XRD data. The zone axis is [100]. Both HRTEM and SAED indicate preferential growth along the *c* axis, which corresponds to the tunnel direction (Figure 4d) with quadratic symmetry.

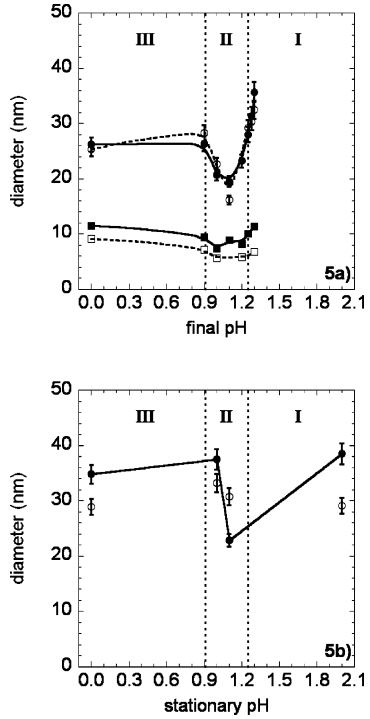

Figure 5. Variations after aging during 7 days at 60 °C (○) or 95 °C (●) of cryptomelane nanowire dimensions. TEM measured diameter vs final pH for method A (a) and stationary pH for method B (b). Crystallite diameter obtained using XRD and the Debye−Scherrer formula at 60 °C (□) or 95 °C (■).

The crystallite diameter obtained by method A and evaluated by XRD (Figure 5a) is of approximately 10 nm, which is smaller than the diameter observed by TEM. Such a difference between TEM and XRD data suggests the presence of defects in lateral directions.

The diameter of particles obtained at 60 and 95 °C has been evaluated from size histograms (Supporting Information) and is reported as a function of final pH (Figure 5a) for method A and stationary pH (Figure 5b) for method B. The error bars correspond to the experimental error on the mean value. In parallel, standard deviations of diameter (Figure 8a) and length (Figure 8b) are indicators of the sample polydispersity and are higher for method B than for method A. It indicates broader size distribution for method B. This could be caused by the lower rate of reactants mixing with method B or the higher concentration of K^+ ions obtained by addition of KOH solution to fix the pH value. The correspondence between final and initial pH and the diameter variation as a function of initial pH for method A is given in Supporting Information. No temperature dependence of diameter is observed for method A (Figure 5a). Three domains are considered for both methods: pH > 1.25 (I), 1.25 > pH > 0.9 (II), and pH < 0.9 (III). In domain I, a decrease of diameter is observed upon decreasing pH (from 36 to 28 nm for final pH ranging from 1.3 to 1.25 with method A). Then, diameter reaches a minimum in domain

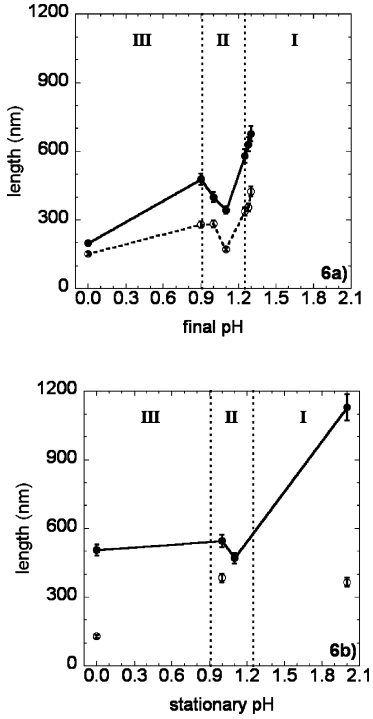

Figure 6. Variations after aging during 7 days at 60 °C (○) or 95 °C (●) of cryptomelane nanowire dimensions. TEM measured length vs final pH for method A (a) and stationary pH for method B (b).

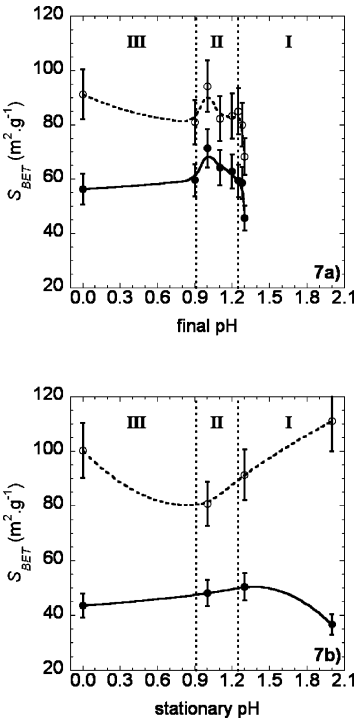

Figure 7. Variations after aging during 7 days at 60 °C (○) or 95 °C (●) of cryptomelane nanowire textural properties. Variation of specific area (S_{BET}) of cryptomelane nanowires synthesized with methods A (a) and B (b).

II (18 nm at final pH 1.1 with method A). Finally, diameter increases again reaching a plateau in domain III (26 nm for final pH < 0.9 with method A). Similarly, length variation upon decreasing pH has been studied (Figure 6). It decreases in domain I, reaches a local minimum in domain II, and decreases again in domain III.

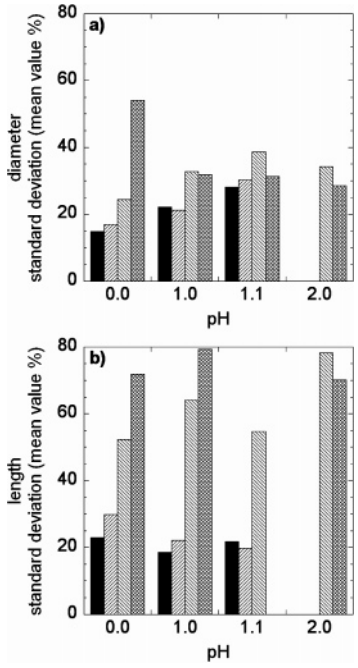

Figure 8. Standard deviations (as percentage of the mean value) of some TEM measured diameters (a) and lengths (b) of cryptomelane nanowires obtained from method A at 95 °C (solid bars) and 60 °C (bars filled with "////"), or from method B at 95 °C (bars filled with "\\\\") and 60 °C (bars filled with criss-cross pattern).

The variation of particle size is confirmed by specific area (S_{BET}) measurements using the BET method (Figure 7). At 95 °C for methods A and B and 60 °C for method A, S_{BET} shows a maximum approximately in domain II. This is approximately 70 and 50 $m^2 \cdot g^{-1}$ at 95 °C for methods A and B, respectively, and 90 $m^2 \cdot g^{-1}$ at 60 °C for method A. These observations are consistent with thinner particles as deduced from Figure 5. S_{BET} is higher at low temperature with shorter nanowires. The high value of S_{BET} at stationary pH 0.0 and 60 °C with method B could be due to high polydispersity of the sample (Figure 8) and predominant contribution of the smallest nanoparticles of the size distribution (15 nm width, 40 nm length), even if the mean size is higher (30 nm width, 125 nm length). In parallel, the samples obtained at stationary pH 2.0 and 60 °C exhibit high specific area in relation with the high polydispersity (Figure 8) and small mean dimensions observed Figures 5b (30 nm width) and 6b (400 nm length), with predominant contribution of small nanowires (20 nm width, 80 nm length). Combining acidity and temperature conditions provides fine control of the BET surface which varies from approximately 35 to 120 $m^2 \cdot g^{-1}$. BET surfaces higher than 100 $m^2 \cdot g^{-1}$ are among the highest reported.[7]

(3) Lateral Growth. Figure 9a shows particles obtained at 60 °C and clearly reveals that nanowires are composed of approximately 10 nm width primary nanorods aggregated along the lateral faces. This observation is consistent with XRD data because crystallite width is of the order of the primary particle diameter. HRTEM Figure 9b was performed on a secondary particle formed by aggregation between two primary particles. Indexed (110) lattice fringes running along the nanowire axis in Figure 9b are identical for both primary particles. This indicates good alignment of the primary

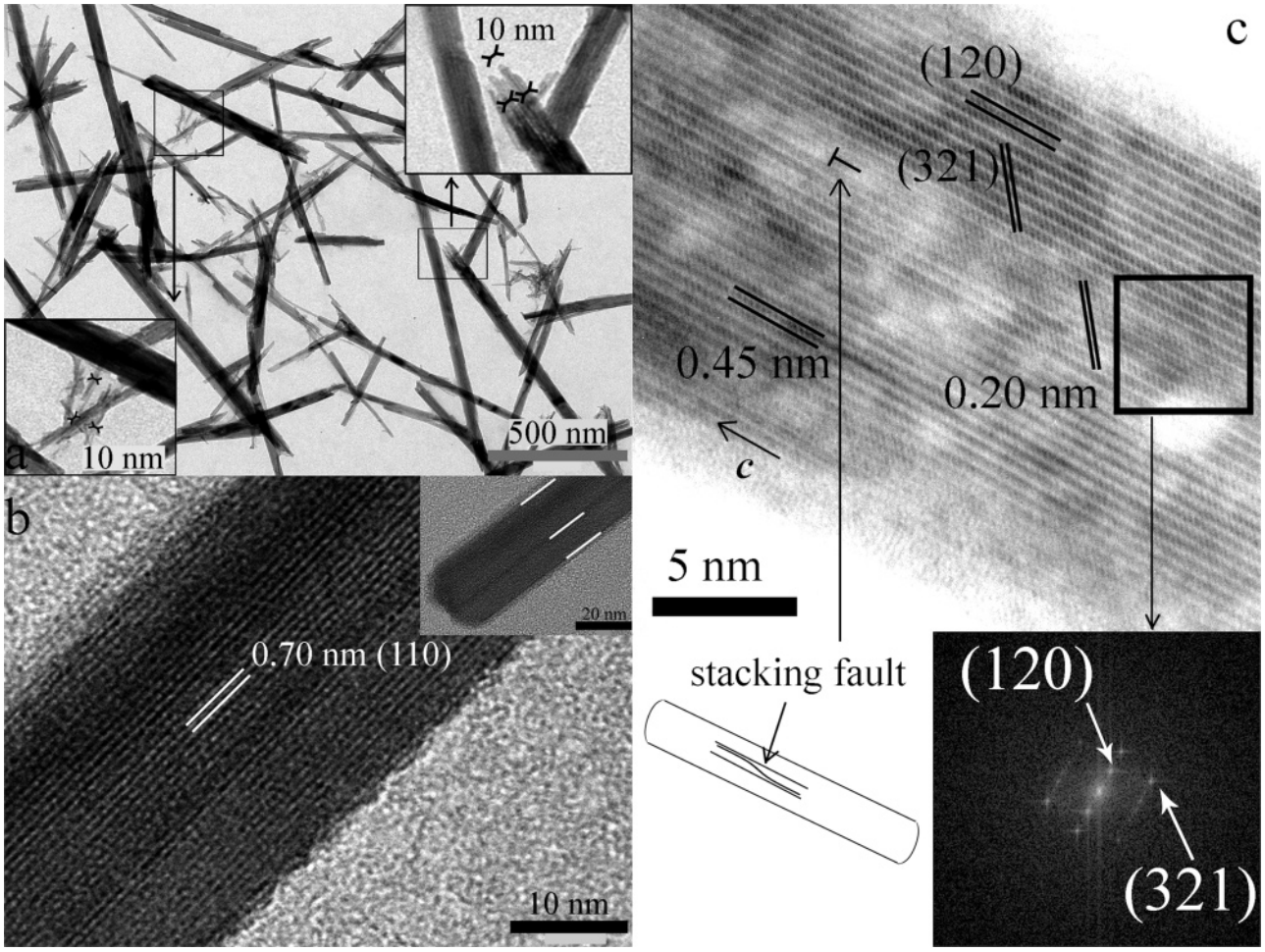

Figure 9. TEM and HRTEM micrographs of cryptomelane nanowires synthesized with method B after aging at 60 °C with stationary pH 2.0, aging time 7 days (a). Method A after aging at 95 °C with initial pH 6.0, aging time 1 day (b). Method A after aging at 95 °C with initial pH 0.0, aging time 7 days (c). FFT showing the good crystallinity of a secondary nanowire.

nanorods along a direction perpendicular to the wire axis. The same situation is observed on HRTEM Figure 9c for the (120) planes. Nevertheless, Figure 9c also reveals a stacking fault of the (120) planes along the wire axis. The formation of such a defect is commonly observed for aggregation driven growth at the interface between primary particles.[33] Moreover, (321) lattice fringes are continuous from both edges of the nanowire. This indicates good alignment of the primary nanorods along the longitudinal axis. Fast Fourier transform (FFT) analysis confirms the good orientation of the primary nanorods which are oriented in both perpendicular and parallel directions to the *c* axis. Aggregation then seems to occur via the oriented attachment mechanism.[24] Single-crystal primary nanorods aggregate in an ordered manner by incorporation of defects at primary particle boundaries and form secondary particles, or mesocrystals.[34] The attachment mechanism is little dependent on temperature as mentioned above for TEM diameter.

Discussion

(1) Precursor to Cryptomelane Structuring. Suib et al. proposed phase ordering to occur by MnO_6 octahedra migration in the disordered precursor.[4] In parallel, using TEM and XRD experiments, Wang and Li proposed that the evolution from birnessite to cryptomelane under hydrothermal conditions occurred through the formation of birnessite nanotubes by rolling of ill-defined sheets.[20] Such reaction intermediates cannot be observed in our low-temperature route synthesis because the precursor is not enough ordered to form lattice fringes when observed by HRTEM. MnO_6 octahedra sheets should likely rearrange and link themselves to each other to form the tunnel structure. Whether this transformation occurs by solid reorganization or by diffusion in solution is not solved for both disordered and lamellar solid precursor.[4,20] Nevertheless, high proton concentration (pH < 2), required for precursor to undergo transformation into cryptomelane, seems in favor of a dissolution−crystallization process. Recently, Suib et al. used in situ synchrotron XRD to investigate phase transformation from birnessite to TMO-1 β-MnO_2 pyrolusite.[19] They observed that sheets connect to each other in the early moments of the reaction to form the intermediate ramsdellite phase with 1×2 octahedra tunnels. Then the structure collapses and leads to the smaller 1×1 tunnels of pyrolusite. Similar in situ investigations could provide useful information to understand the phase transformation described in this report. Especially, it would enable the understanding of

(33) Penn, L. R.; Banfield, J. F. *Science* **1998**, *281*, 969−971.
(34) Cölfen, H.; Antonietti, M. *Angew. Chem., Int. Ed.* **2005**, *44*, 5576−5591.

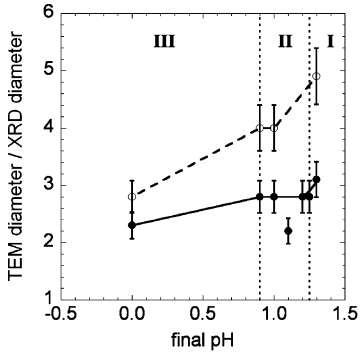

Figure 10. Variation of the ratio between TEM measured nanowires diameter and XRD measured crystallite diameters with acidity after aging 7 days at 60 °C (○) or 95 °C (●) for synthesis method A.

whether the process is straightforward or if it involves intermediate open structures such as 3 × 3 or 2 × 3 TMO. However, a detailed study of the transformation is not the purpose of this report.

(2) Morphology Control of Nanowires. The ratio between TEM measured and XRD measured diameters for method A (Figure 10) gives an indication of the number of primary particles incorporated in a secondary particle in a lateral direction. Its value is higher at 60 °C and indicates that more boundaries between primary nanorods are observed at low temperature. The ratio is approximately constant, equal to 2.5 at 95 °C, and decreases by steps from 5 to 3 at 60 °C in agreement with the decrease of the TEM diameter (Figure 5a). By decreasing the pH in domain III, the ratio continuously decreases, reaching 3 and 2.2 at 60 and 95 °C, respectively, whereas the TEM diameter increases again (Figure 5a). This surprising behavior is linked to the increase of the crystallite diameter measured by XRD. This indicates that the monocrystalline primary nanorods are well ordered together at low pH in the mesocrystal. The iso-electric point of K-TMO-2 nanoparticles has been evaluated to 2.8 by ζ potential measurements. According to mobility measurements and calculations using the MUSIC model,[35] the lateral surface positive charge increases strongly at $1 < pH < 1.5$ and is maximal for pH below approximately 1. The DLVO (Derjaguin−Landau−Verwey−Overbeek) theory provides a general framework to understand the diameter variations by considering the electrostatic repulsive potential component.[36−38] This interaction is governed by two main factors: the surface potential and the Debye length. The latter is greatly influenced by the ionic strength of the aqueous medium: the higher the ionic strength, the smaller the Debye length. Because interactions are more repulsive for higher surface potential (e.g., surface charge) and longer Debye length, both factors have opposite effects as pH is decreased: the ionic strength is increased together with the surface charge. Taking into account the concentration of potassium ions, of protons formed by the precipitation reaction, and the initial acidity, the ionic strength is evaluated to 1.3×10^{-1}, 2.2×10^{-1}, and 1.2 mol·L^{-1} at final pH values of 1.3, 0.9, and 0.0, respectively. Therefore, the separation into three domains in Figure 5 can be tentatively explained: domain I (pH > 1.3) corresponds to weakly charged surfaces and too low electrostatic repulsions to prevent aggregation between nanorods. Domain II (final pH between 0.9 and 1.3) is characterized by highly charged surfaces and higher electrostatic repulsions between positively charged primary particles. This results in limited aggregation and diameter decrease. Domain III (below pH 0.9) is characterized by high ionic strength which reduces the Debye length and results in low electrostatic repulsions because of a screening effect, even if the surface charge is maximal. Then the diameter increases again. Secondary nanowires observed by TEM after 7 days are often monocrystalline ones without evidence of a polycrystalline nature. This can be explained by coarsening during aging, which leads to reconstruction of boundaries between primary single crystals and smoothing of the surfaces. This process should occur at a longer time scale than oriented attachment as previously described by Huang et al. for ZnS nanoparticles growth.[25] Ostwald ripening is made easier in an acidic medium where Mn species are more soluble. This explains the small number of primary particle boundaries observed in a strong acidic medium as deduced from the low value of the ratio (Figure 10). Low temperature limits coarsening and results in more observable boundaries as observed at 60 °C. Even if coarsening seems to occur at high temperature, the non-monotonous diameter variation with pH (Figure 5) can only be explained by an aggregation driven growth. Therefore, the oriented attachment remains the main lateral growth process which is responsible for diameter variation under modification of the acidic conditions.

Given the higher impact of temperature on longitudinal growth and the absence of evidence by TEM observation of aggregation along the nanowire axis, growth along the nanowire axis proceeds by another mechanism. The dissolution−crystallization process is temperature dependent because rising temperature increases the solubility of the Mn species, which is in agreement with the increase of length with temperature. Furthermore, this mechanism is acidity dependent for two opposite reasons: on one hand the solubility of Mn species is increased in a highly acidic medium, thus promoting the growth stage. On the other hand, proton chemisorption stabilizes surfaces, thus stabilizing small particles with high surface area and limiting the growth stage.[39] Considering the longitudinal growth along the *c* axis indicates that (001) faces are the most energetic ones. Stabilization by proton adsorption should occur and have great impact on the final nanowire morphology by limiting longitudinal growth. This should result in smaller length as in domain III in Figure 6. Coarsening is thus believed to be the major mechanism that occurs during longitudinal growth (longitudinal growth route 1 in the general scheme described in Figure 11). The decrease of length in domain II could be explained by the limited lateral aggregation. Indeed, when

(35) Hiemstra, T.; Venema, P.; Riemsdijk, W. H. V. *J. Colloid Interface Sci.* **1996**, *184*, 680−692.
(36) Derjaguin, B. V.; Landau, L. *Acta Physicochim. URSS* **1941**, *14*, 633−662.
(37) Vervey, E. J.; Overbeek, J.-T. G. *Theory of The Stability of Lyophobic Colloids*; Elsevier: Amsterdam, 1948.
(38) Israelachvili, J. *Intermolecular and Surface Forces*; Academic Press: London, 1992.
(39) Pottier, A.; Cassaignon, S.; Chaneac, C.; Villain, F.; Tronc, E.; Jolivet, J.-P. *J. Mater. Chem.* **2003**, *13*, 877−882.

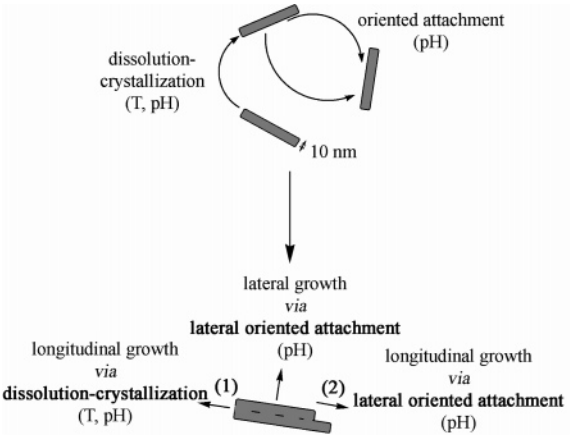

Figure 11. Growth scheme for longitudinal and lateral directions from primary nanorods.

lateral aggregation occurs easily, primary nanorods aggregate randomly along the wires direction and a longitudinal growth is expected (longitudinal growth route 2 in Figure 11). It was reported that longitudinal growth of oxide nanorods could also proceed by oriented attachment of nanodots,[26,40] but such a mechanism was not observed in the present study. Another longitudinal growth mechanism could be end-to-end oriented attachment of primary nanorods,[41] but no evidence of such aggregation was obtained by TEM observation.

(40) Penn, R. L.; Erbs, J. J.; Gulliver, D. M. *J. Cryst. Growth* **2006**, *293*, 1−4.
(41) Dessombz, A.; Chiche, D.; Davidson, P.; Panine, P.; Chanéac, C.; Jolivet, J.-P. *J. Am. Chem. Soc.* **2007**, *129*, 5904−5909.

Conclusion

A new low-temperature synthesis of 1D manganese oxide in aqueous medium has been developed. This soft chemistry route leads quantitatively to pure cryptomelane nanowires. Crystallization occurs by transformation of a disordered precursor in acidic medium. Aging parameters are the key stones for morphology tailoring. Longitudinal and lateral growth proceed by different mechanisms that can be controlled by adjustment of the acidity and the temperature. Morphology control of 1D TMO-2 should provide interesting nanosystems to investigate their catalytic and electrochemical properties. Finally, this study provides new insights in manganese oxide formation reaction and highlights a new growth scheme of 1D oxide nanostructure formation and size tailoring.

Acknowledgment. The authors would like to thank Sophia Khan and Tamar Saison for experimental support, Dr. Patricia Beaunier and Dr. Dominique Jalabert for TEM and HRTEM observations, and Dr. François Ribot for fruitful discussions.

Supporting Information Available: Correspondence between initial and final pH for method A, variation of TEM measured diameter and length versus initial pH for method A, and some histogram plots of diameter and length for method A (PDF). This information is available free of charge via the Internet at http://pubs.acs.org.

CM071654A